Wind Stress Curl and Wind Stress Divergence Biases from Rain Effects on QSCAT Surface Wind Retrievals

RALPH F. MILLIFF AND JAN MORZEL

Colorado Research Associates, NorthWest Research Associates, Boulder, Colorado

DUDLEY B. CHELTON AND MICHAEL H. FREILICH

College of Ocean and Atmosphere Sciences, Oregon State University, Corvallis, Oregon

(Manuscript received 1 September 2003, in final form 2 February 2004)

ABSTRACT

Surface vector wind datasets from scatterometers provide essential high-resolution surface forcing information for analyses and models of global atmosphere–ocean processes affecting weather and climate. The importance of realistic amplitude, high-wavenumber, surface wind forcing from scatterometer data has been demonstrated in a variety of ocean modeling applications. However, the radar backscatter signal from which surface vector wind estimates are retrieved is attenuated and/or contaminated in heavy rain. The QuikSCAT (QSCAT) dataset flags rain-contaminated wind vector cells where retrievals are either highly uncertain or not available. Zonal and annual averages of wind stress curl and divergence for 2000, 2001, and 2002 are derived and compared across three surface wind datasets: QSCAT only, reanalysis winds from the National Centers for Environmental Prediction (NCEP reanalysis), and blended QSCAT+NCEP. Missing QSCAT surface wind retrievals due to rain contamination lead to statistically significant discrepancies of up to 50% in the implied Sverdrup transports in subtropical and subpolar gyre regions of the Northern and Southern Hemispheres. Dataset-to-dataset wind stress divergence amplitude differences due to rain contamination are also large in the midlatitude storm track regions. Discrepancies occur in the Tropics due to rain contamination effects on QSCAT data and due to high-wavenumber deficiencies in the NCEP reanalysis winds. In addition, NCEP operational forecast model surface wind analyses (NCEP–FNL) have been trilinearly interpolated to the QSCAT wind vector cell locations and sample times. The NCEP–FNL winds are not affected by rain, so it is possible to compare NCEP–FNL-interpolated surface wind fields and related quantities calculated with and without wind vectors at the rain-flagged wind vector cell locations. When all locations are included, wind stress curl amplitudes are found to be skewed toward cyclonic curl in both hemispheres. Vectors at rain-flagged locations in both hemispheres are also skewed toward large-amplitude, cyclonic curls. This is because midlatitude synoptic systems are the meteorological sources of large-amplitude cyclonic curls, as well as the places where the rain-flag bias in wind stress curl is largest. Blended QSCAT+NCEP surface winds ameliorate the rain-flag-induced biases in zonal averages of wind stress curl and wind stress divergence, while retaining high-wavenumber properties of the scatterometer winds. Evidence to support rain-flag algorithm refinement for high wind speeds is presented.

1. Introduction

The curl of the surface wind stress is a direct and often dominant source term in the vorticity budget of the upper ocean, with implications for mesoscale and basin-scale circulation. As the sophistication and resolutions of regional and global ocean general circulation models increase, they become increasingly sensitive to accurate surface wind stress curl forcings. Ocean vector wind retrievals from spaceborne scatterometer systems provide essential high-wavenumber data necessary to meet wind stress curl requirements of modern ocean models.

Surface wind stress divergence in conjunction with sea surface temperature (SST) provide indications of air–sea interaction and the related stability of the marine atmospheric boundary layer. For example, Chelton et al. (2001) employed Tropical Rainfall Measuring Mission (TRMM) Microwave Imager SST data and surface wind fields from the National Aeronautics and Space Administration (NASA) QuikSCAT (QSCAT) scatterometer to demonstrate a close ocean–atmosphere coupling in the eastern tropical Pacific in association with tropical instability wave perturbations of the SST front on the north side of the equatorial cold tongue. The same coupled ocean–atmosphere processes are evident over SST fronts in midlatitude regions (O'Neill et al.

Corresponding author address: Dr. Ralph F. Milliff, Colorado Research Associates Division, NorthWest Research Associates, Inc., 3380 Mitchell Lane, Boulder, CO 80301.
E-mail: milliff@colorado-research.com

2003; Nonaka and Xie 2003; Chelton et al. 2004; P. Niiler 2003, personal communication). Daily, global satellite-based observations of the joint distributions of surface wind stress divergence and SST could provide rigorous validation scenarios for high-resolution coupled ocean–atmosphere models that are currently being developed.

Scatterometer observing systems cannot retrieve accurate vector winds where it is raining. This paper identifies systematic biases in wind stress curl and wind stress divergence fields derived from scatterometer surface wind retrievals that are due to the observations missing from the scatterometer record, mostly due to rain. Zonal average measures of these biases can be overcome in large part by blending weather center surface wind reanalyses with coincident scatterometer surface wind retrievals.

The paper is organized as follows. Five surface wind datasets are introduced in the next section. Wavenumber spectral properties for these datasets are reviewed to serve as bases for comparisons throughout the paper. In section 3, we examine and compare a variety of distributions and summaries of wind stress curl properties for each of the datasets. Synoptic settings relevant to the wind stress curl differences are described in section 4. Section 5 demonstrates the wind stress divergence bias due to rain. The ameliorating advantages of blended scatterometer and reanalysis surface winds are discussed in section 6, and a summary is provided in section 7.

2. Surface wind datasets

We will compare and contrast wind stress curl computed from five different surface wind datasets introduced in this section. For the purposes of this paper, the surface wind datasets are referred to as QSCAT only, National Centers for Environmental Prediction (NCEP) Reanalysis, blended QSCAT+NCEP, Oregon State University (OSU)–NCEP–FNL–no rain, and OSU–NCEP–FNL–rain, where FNL refers to the NCEP operational forecast model surface wind analyses.

a. QSCAT only

The QSCAT-only winds derive from the QuikSCAT spaceborne scatterometer mission launched in June 1999. QSCAT data processing began in July 1999, and the system continues to operate well. The scatterometer instrument aboard QSCAT is a SeaWinds system, which transmits a radar signal of known frequency and polarizations to the sea surface, and then measures the backscattered radar return. The radar backscatter is a function of sea surface roughness, the angle of incidence of the transmitted pulse, and other parameters. Several returns, for different geometries and radar properties (e.g., polarization), are used from the same patch of ocean surface, or wind vector cell (WVC), to retrieve estimates of wind speed and wind direction by inverting an empirical model function. The model function relates speed and direction of the equivalent neutral stability wind at 10 m above the sea surface to the geometric and radar properties affecting backscatter. The essential description of the vector wind retrieval process is the SeaWinds Algorithm Theoretical Basis Document (Freilich 1996). Useful summaries are also available in the QSCAT science data product user's manual (National Aeronautics and Space Administration 2001). (The QSCAT surface vector wind data products and documentation are available online from the Jet Propulsion Laboratory, PO-DAAC at http://podaac.jpl.nasa.gov/cgi-bin/dcatalog/fam_summary.pl?ovwtqscat.) In this study, we use the direction interval retrieval with threshold nudging (DIRTH) version of the QSCAT surface wind retrievals as described by Stiles (1999). The level 2B DIRTH vector wind product has become the de facto standard product for many science applications of QSCAT winds.

The QSCAT vector winds are derived at a resolution of 25 km, within a 1600-km-wide swath that spans the satellite ground track along its polar orbit flight path. The QSCAT orbit is inclined 98.6°, and the spacecraft flies at an altitude of 803 km. The orbital period is about 101 min, so that about 14.3 orbits are completed each day. Ocean surface winds are retrieved for approximately 90% of the ice-free global ocean every 24 h. QSCAT winds have been validated in field comparisons with in situ buoys and weather center surface wind analyses (e.g., Ebuchi et al. 2002; Freilich and Vanhoff 2003; Draper and Long 2002). The vector winds from QSCAT are accurate in calibrations with in situ buoys to well within the mission requirements of wind speed within 2 m s^{-1} rms, and wind direction within 20° rms (National Aeronautics and Space Administration 2001).

A second SeaWinds system was launched in late 2002 aboard the *Midori-II* spacecraft of the Japanese Space Agency (NASDA).[1] *Midori-II* failed on orbit in late October, and the SeaWinds system was lost along with all other instruments on the platform. However, a surface wind data record from 10 April to 24 October 2003 was obtained from the SeaWinds system aboard *Midori-II*. The *Midori-II* equator-crossing times coordinated with QSCAT such that surface winds were retrieved for 90% of the ice-free global ocean in about 12 h. The combined SeaWinds data from QSCAT and *Midori-II* define the so-called Tandem Mission surface vector wind data record. Work in progress will quantify the impact and science advantages of the Tandem Mission. For a review of scatterometer development history, and the prospects for continuous global surface vector wind data records from spaceborne scatterometers, see Milliff et al. (2001).

[1] NASDA renamed the *ADEOS-II* spacecraft after the SeaWinds scatterometer and other instruments were commissioned on orbit.

RAIN FLAGS

The emitted microwave pulse and the backscatter from the ocean surface at the SeaWinds frequency (13.4 GHz, Ku band) are attenuated and backscattered by heavy rain. In addition, raindrops create a sea surface roughness not related to the surface wind, thereby confounding the model function inversion necessary to retrieve surface wind from radar backscatter. The QSCAT processing includes two estimates of rain contamination for each WVC retrieval. The estimates are based in part on how well the radar returns fit the geophysical model function, and are expressed as either a ''multidimensional histogram'' rain probability (MUDH; Huddleston and Stiles 2000) or as an ''empirically normalized objective function'' rain index (ENOF; Mears et al. 2000).

In the QSCAT level 2B data, a binary rain-flag determination (e.g., rain contaminated or not) is made for each WVC based on the MUDH algorithm. This flag was used in our analyses to identify rain-contaminated WVCs. In comparisons with Special Sensor Microwave Imager (SSM/I) rain retrievals, the performance of the MUDH algorithm was found to depend on wind speed. Assuming the SSM/I retrievals are ''truth,'' the ''false alarm'' rate (QSCAT rain flagged, SSM/I not rain flagged) was 2%–3% for all QSCAT rain-flagged WVCs. The ''missed rain'' rate (QSCAT not rain flagged, SSM/I rain flagged) was 26%–39% for wind speeds 3–30 m s^{-1} (Huddleston and Stiles 2000). The rain-flag determination criteria for active scatterometer systems remains a subject of research and debate within the vector wind retrieval community. The analysis here bolsters a case for continued rain-flag algorithm development for these systems.

b. NCEP reanalysis

The reanalysis winds from the NCEP reanalysis continue from the 40-yr (1957–96) NCEP–NCAR Reanalysis described in Kalnay et al. (1996). Zonal and meridional components of the 10-m wind are analyzed using the forecast model and Climate Data Assimilation System (CDAS) versions fixed for the reanalysis project. The 10-m wind component data are available for the globe at 0000, 0600, 1200, and 1800 UTC each day, on Gaussian grids corresponding to a T62 spectral truncation (about 2.5° resolution in the surface fields). (A growing archive is maintained online at http://dss.ucar.edu/datasets/ds090.0/.)

The NCEP reanalysis winds are included in the comparisons here because they are often used in climate-scale research. Even though resolution and analysis procedures in the latest NCEP operational surface wind products are enhanced relative to the NCEP reanalyses, the latter set provides consistency over longer time scales that are required in a so-called climate data record (e.g., see National Research Council, Space Studies Board 2000).

Scatterometer surface winds are not assimilated in CDAS, so the NCEP reanalysis winds used here do not contain the influence of surface winds derived from scatterometer observations (S. J. Worley 2002, personal communication). Later reanalysis efforts will undoubtedly include scatterometer winds as part of the input data. The properties of the particular numerical models and data assimilation systems used in those efforts will determine whether or not important large-amplitude, small-scale (high wavenumber) signals inherent in the scatterometer data will have realistic representations in new reanalysis products.

c. Blended QSCAT+NCEP

A blend of QSCAT and NCEP reanalysis surface wind datasets is motivated by (a) realistic high-wavenumber properties in the former; and (b) the long-term dataset stability, regular gridding, and 4-times-daily availability, of the latter. The wavenumber spectral properties of QSCAT and blended QSCAT+NCEP surface winds are discussed in detail at the end of this section. The blending method developed in Chin et al. (1998) for the NASA scatterometer (NSCAT) has been extended to the entire QSCAT record to create the blended QSCAT+NCEP surface wind dataset available at http://dss.ucar.edu/datasets/ds744.4/.[2] This dataset consists of global 6-hourly maps at 0.5° resolution and is updated roughly every 6 months as the QSCAT mission continues.

Over most of the ocean surface, the blended QSCAT+NCEP winds are identical to QSCAT-only winds. In the gap regions between QSCAT swaths and for the measurement locations where QSCAT data are absent, the blended QSCAT+NCEP winds consist of a stochastic enhancement of NCEP reanalysis at high wavenumbers in the spectral amplitudes of the zonal and meridional winds. The spectral slopes in the enhancement are constrained to be consistent with regional and monthly power-law behavior that is taken from the coincident QSCAT data. To maximize coverage when data from only a single scatterometer are available, each 6-hourly global NCEP reanalysis field is blended with the most recent 12 h of QSCAT data. This window can be reduced to 6 h, commensurate with the analysis time steps, for the period of the Tandem Mission. Simultaneous observations from two scatterometer systems are expected to diminish the influence of the background winds due to NCEP reanalyses as the blended product is tested for the period of the Tandem Mission.

[2] We use version 1 of the blended QSCAT+NCEP in this study. Version 1 is based on the QSCAT DIRTH winds and excludes all rain-flagged WVCs. Based in part on the results to be described here, version 4 of the blended QSCAT+NCEP winds has recently been made available. Version 4 improves on wavelet statistics in the blending method, and includes rain-flagged QSCAT DIRTH WVCs for wind speeds ≥15 m s^{-1}. Product descriptions for all versions of the blended QSCAT+NCEP winds are available online.

While most of the spectral enhancement in the blended QSCAT+NCEP occurs for locations between the QSCAT swaths, it is important for the purposes of this paper to emphasize that the rain-flagged WVCs in the QSCAT record are also supplemented in the blending method.

d. Oregon State University–interpolated NCEP–FNL

Surface winds from the NCEP operational analyses (so-called final analysis or NCEP–FNL) have been interpolated in space and time to the WVC locations for each QSCAT swath. The NCEP–FNL is the final assimilation and forecast run in each operational cycle. The output field of interest includes 6-h analyses of the 10-m winds available at 0000, 0600, 1200, and 1800 UTC, after late-arriving conventional and satellite data have been assimilated in the Global Data Assimilation System (GDAS) that is the current operational standard at NCEP. The NCEP–FNL winds are converted from the spectral representation of the forecast model to the 1° grid for dissemination. Here, they have been trilinearly interpolated to the QSCAT WVCs for each orbit in the QSCAT data record; including those WVCs for which the rain flag indicates that no vector wind retrieval was obtained, or for which the vector wind retrieval is highly uncertain. We refer to the interpolated winds as OSU–NCEP–FNL to note the distinction with respect to NCEP–FNL on the regular grid.

We have partitioned the OSU–NCEP–FNL into two sets. In the ''rain'' set the interpolated vector winds are retained at all WVCs. In the ''no rain'' set, we exclude interpolated winds at locations that were identified as rain contaminated in the QSCAT retrieval. This makes feasible rain versus no-rain comparisons in the 10-m winds and derived fields, albeit for datasets with spectral properties that differ with respect to winds retrieved from scatterometry. We note that since 15 January 2002, the QSCAT 10-m winds have been used in the GDAS, and therefore have some effect in the NCEP–FNL product since that date.

e. Comparison wavenumber spectra

Figure 1 depicts power spectral density (PSD) versus wavenumber for zonal wind samples from the surface wind datasets introduced in this section. The samples are extracted for each dataset from a region of the North Pacific Ocean (20°–50°N, 180°–220°E). In the case of QSCAT-only and OSU–NCEP–FNL data, along-track segments are 30° long with segment midpoints evenly distributed across the region of interest. For the NCEP reanalysis and blended QSCAT+NCEP winds that occur on regular grids, 30° long meridional segments are drawn at longitudes 180°, 190°, 200°, 210°, and 220°E. The zonal wind samples from all datasets span the year 2000, and spectra shown in Fig. 1 are the averages of spectra computed for segments drawn from the North Pacific region of interest over the entire year. For the OSU–NCEP–FNL case when rain-flagged WVCs were included, the total number of along-track segments used in the average is 7400. The average spectra in the QSCAT-only and OSU–NCEP–FNL ''no rain'' case are based on 3500 different along-track segments. An entire 30° segment was discarded whenever more than one consecutive WVC wind retrieval was missing. Single missing WVC were filled by linear interpolation before spectral decomposition. For the gridded datasets (blended QSCAT+NCEP and NCEP reanalysis) there were 7300 different zonal wind spatial segments contributing to the average spectra.

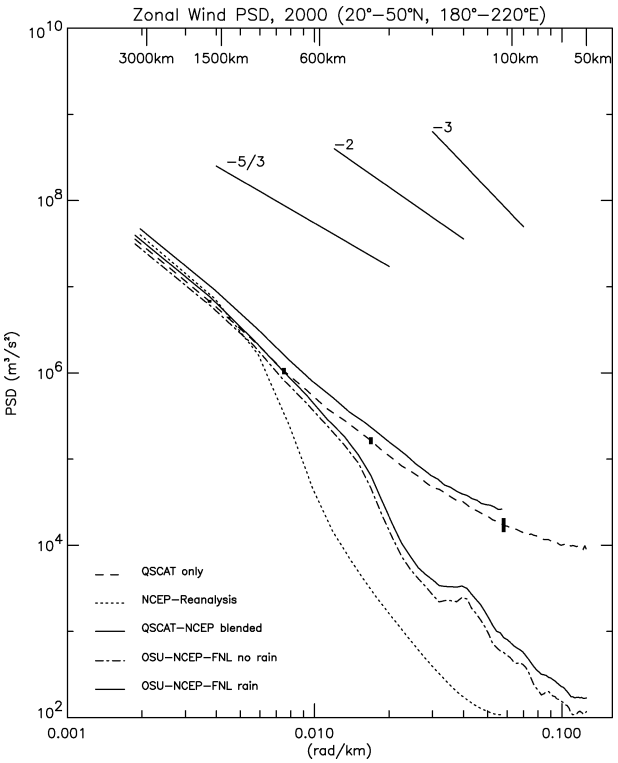

FIG. 1. PSD vs wavenumber spectra for the zonal component of the surface wind in the North Pacific for the calendar year 2000. Spectra are shown for five surface wind datasets introduced in the text: QSCAT-only (dashed line), NCEP reanalysis (dotted line), blended QSCAT+NCEP (solid line), OSU–NCEP–FNL excluding rain-flagged WVCs (dash–dot line), and OSU–NCEP–FNL with rain-flagged WVCs included (dash-3 dot line). Approximate power-law behavior in surface winds from scatterometer observations are well documented. Weather center winds depart from approximate power laws at scales much larger than the highest resolutions of the respective datasets. Bootstrap confidence intervals are indicated on the QSCAT-only dashed line at four different wavenumbers. The QSCAT-only dataset was partitioned into 10 subsets and average spectra were computed for each subset. The vertical bars indicate the range of the 10 subset averages.

The spectra in Fig. 1 serve as a recent example of a wavenumber spectral distinction that is well known in comparing weather center winds (analyses and forecasts), with winds retrieved from scatterometry. Freilich and Chelton (1986) computed wavenumber spectra from

the brief Seasat scatterometer wind dataset for tropical and subtropical regions of the Northern and Southern Hemisphere Pacific Ocean. They noted an approximate k^{-2} power-law relation in surface wind kinetic energy versus wavenumber (k) that extended to very near the Nyquist wavenumbers for that system. In several subsequent studies (cited below), power-law relations have been apparent in scatterometer wind datasets, while a similar power-law relation is not maintained to Nyquist wavenumbers in spectra calculated from weather center winds. In Fig. 1, the wavenumber spectra for NCEP reanalysis winds depart from the power law at scales smaller than 800–1000 km, while for the OSU–NCEP–FNL winds, the departure occurs at scales between 500 and 600 km. In both cases, these spatial scales are many times larger than the grid resolutions on which reanalysis or forecast winds are made available. QSCAT data were not assimilated in the NCEP forecast models in 2000.

Freilich and Chelton (1986) noted the connection between power-law relations in wavenumber spectra from scatterometer winds and theoretical results for isotropic two-dimensional turbulence. Wikle et al. (1999) expanded on this discussion in a paper that built composite wavenumber spectra for the Tropical Ocean Global Atmosphere Coupled Ocean–Atmosphere Response Experiment (TOGA COARE) intensive observation period (IOP) region from combined 10-m wind analyses from NCEP, 10-m winds retrieved from the *European Space Agency Remote Sensing Satellite 1* (*ERS-1*) scatterometer, and high-resolution retrievals of 10-m winds from Doppler radar measurements from aircraft. A $k^{-5/3}$ power law was apparent over three decades in wavenumber for this tropical western Pacific domain. The shallower spectral slope was noted to be consistent with increased effects of an inverse energy cascade driven by an energy source at high wavenumbers, thought to be associated with tropical convection. Patoux and Brown (2001) reiterated some of this earlier work using QSCAT data. Milliff et al. (1999) demonstrated a time and space variability in the spectral slope properties that is also consistent with notions from two-dimensional turbulence. However, the spectral properties in the tropical Pacific as well as midlatitude examples do not exclude interpretations outside two-dimensional turbulence concepts (e.g., breaking internal wave effects). The regional and temporal dependence of the spectral slopes of wavenumber spectra at high wavenumbers form the basis of the blending method used to derive the blended QSCAT+NCEP product described above.

More subtle in Fig. 1 are the distinctions in PSD versus wavenumber as a function of including rain-flagged locations in the analyses. The OSU–NCEP–FNL comparisons (rain versus no rain) demonstrate the magnitude of this distinction in datasets that are systematically deficient in PSD with respect to a power-law relation at moderate to high wavenumbers. The comparison between QSCAT-only and blended QSCAT+NCEP spectra depicts similarly small differences presumably due to the rain/no-rain effect for surface wind datasets with realistic high-wavenumber content. Both cases, including surface wind estimates for rain-flagged WVCs, slightly raise the PSD at all wavenumbers. Bootstrap estimates of confidence intervals on the QSCAT-only spectra are indicated at several wavenumbers by solid bars in Fig. 1. The rain versus no-rain distinction between QSCAT-only and blended QSCAT+NCEP is seen to be significant with respect to these estimates.

3. Wind stress curl

The subtle differences due to rain that were evident in the wavenumber spectra of the previous section are amplified in comparisons of zonal and annual average wind stress curl.

Formulas and methods for computing wind stress curl from scatterometer surface wind retrievals are described in Milliff and Morzel (2001) for the NSCAT system. These same methods are applied here using the QSCAT-only and OSU–NCEP–FNL datasets. The essential features of the protocol are (a) the wind stress curl is computed orbit-by-orbit to ensure that the calculated curl is consistent with the meteorology and is not an artifact of surface wind events that might occur in the same place at different times; and (b) to the extent feasible, high-wavenumber fidelity of the scatterometer system is preserved by using 50-km bins to accumulate surface wind stress for each orbit, and an overlapping grid of spatial differences on 50-km centers to compute curl (see Milliff and Morzel 2001 for details).

Milliff and Morzel (2001, see their Fig. 9) demonstrate that wind stress curl is highly intermittent and amplitudes can change abruptly by two or three orders of magnitude, in contrast to much smaller variability in the surface wind velocity field itself. Orbit-by-orbit processing permits the detection of large and intermittent wind stress curl events in the data. We will see (section 3) that rain-flagged WVCs concentrate in subregions of synoptic systems that are characterized by large-amplitude, intermittent wind stress curl. In order to accurately represent wind stress curl in the fine spatial scales consistent with synoptic structures, we required wind stress bin counts to be as uniform as possible within each orbit. This leads to the overlapping 50-km bins described above. For 4-yr averages of the wind stress curl field from QSCAT, Chelton et al. (2004) have successfully pushed this resolution to 25 km.

Wind stress curl (and divergence fields to be discussed later), as derived here from scatterometer surface wind datasets, are inherently noisy fields. Contributions to the noise come from amplification of measurement noise through the derivative operation, the space–time irregularities in the swath sampling, and the effects of energetic subgrid geophysical processes in the surface wind observations. Milliff and Morzel (2001) quantify the wind stress curl noise in terms of a gradient root-

mean-square (grms) error. Zonal integrals of grms estimates for NSCAT are comparable in magnitude to the approximate confidence intervals to be described in Fig. 2 for the QSCAT-only dataset.

Wind stress curl calculation is more straightforward for regularly gridded data. An overlapping 0.5° spatial resolution is preserved in wind stress curl fields computed at 6-h intervals from the blended QSCAT+NCEP and NCEP reanalysis winds. In a preparatory step for blending with QSCAT, NCEP reanalysis winds are splined to a 0.5° grid (see Chin et al. 1998). The wind stress curl averages shown here are computed from the 0.5° representations of the NCEP reanalysis.

a. Zonal, annual averages

The well-known Sverdrup balance relates zonal integrals of the wind stress curl to ocean transport streamfunction, under linear, inviscid, and β-plane assumptions. The balance is given by (e.g., Pedlosky 1998)

$$\Psi_{\mathrm{Sv}} = \frac{-1}{\rho_o \beta} \int_{x_{\mathrm{E}}}^{x} \nabla \times \boldsymbol{\tau}\, dx', \qquad (1)$$

where Ψ_{Sv} is the Sverdrup transport streamfunction, β is the planetary vorticity term, and ρ_o is a reference density. The wind stress curl is given by $\nabla \times \boldsymbol{\tau}$, for horizontal wind stress vector $\boldsymbol{\tau}$. The line integral in (1) is commonly computed in the westward direction from an eastern ocean boundary x_{E} to the point x where the transport is approximated. The meridional ocean transport is controlled by the zonal integral of the wind stress curl. In this section we evaluate zonal averages of this quantity for the surface wind datasets introduced above. Implied Sverdrup transport differences are directly proportional to the differences in the averages of wind stress curl along each latitude.

Figure 2 depicts zonal and annual averages of the wind stress curl for the years 2000 (Fig. 2a), 2001 (Fig. 2b), and 2002 (Fig. 2c), as derived from the QSCAT-only (blue), blended QSCAT+NCEP (red), and NCEP reanalysis (black) winds. The green curve in Figs. 2a–c will be discussed later. Figure 2d plots data volumes as functions of latitude for the blended QSCAT+NCEP and NCEP reanalysis averages (top curve), and for the QSCAT-only average (bottom curve) for the year 2000. In the cases of regularly gridded datasets, the data volumes versus latitude reflect the number of ocean data points. For the QSCAT-only case, the number of data points is convolved with the sampling characteristics of the polar-orbiting platform (e.g., interswath gaps in coverage are largest at the equator, and swath overlap areas increase with latitudes above about 48°).

Bootstrap confidence interval estimates for the equator and latitudes ±20°, ±30°, and ±50°, are indicated in Figs. 2a–c for the QSCAT-only wind stress curl averages. These estimates take into account the spatial autocorrelation in the zonal averages at each latitude as follows. Lagged covariance estimates were computed for the annual average spatial series at the selected latitudes for spatial lags corresponding to each of the nearest 12 wind stress curl bins (i.e., a sequence of spatial lags from ±0.5° to ±6° of longitude, incremented by 0.5° in each direction). The average lag-covariance functional shapes were roughly similar for all latitudes, while absolute values varied as functions of latitude. At all latitudes, covariance functions decreased monotonically with increasing spatial lags, to inflection points where a minimum positive covariance was more or less maintained out to large spatial lags. Covariance function inflection points occurred at spatial lags of about 2.5°, or five wind stress curl bin widths. Minimum correlation amplitudes at this range did not exceed 0.5, and were more commonly smaller. Given this, we computed five new estimates of the zonal mean for the selected latitudes, offsetting the starting longitude by one, and using every fifth wind stress curl bin in the spatial series. The spread of the five different zonal means is indicated by the black solid bars in Fig. 2. Following the experience in Milliff and Morzel (2001), we have assumed that wind stress curl bin averages are not strongly correlated in time over the minimum repeat sample interval of about 12 h.

The confidence interval estimates at the selected latitudes suggest that annual zonal averages of wind stress curl from QSCAT-only data differ significantly from averages computed from coarse-resolution NCEP reanalysis winds as well as from the blended QSCAT+NCEP winds. The average wind stress curl traces for QSCAT-only and blended QSCAT+NCEP exhibit variabilities on scales of about 1° latitude, suggesting that this variability arises from the wind field signals resolved in the scatterometer observations. Consistent with its coarser native resolution and the absence of any scatterometer influence, the NCEP reanalysis curves are smooth at the 1° scale.

While some year-to-year differences are evident, the characteristics of the distinction between wind stress curl averages from QSCAT-only winds and those from NCEP reanalysis or the blended QSCAT+NCEP winds are very similar over the 3 yr depicted here (Figs. 2a–c). The largest differences occur at latitudes corresponding to the subtropical gyres in both hemispheres. QSCAT-only wind stress curl average amplitudes in these latitudes (e.g., centered on say 40°S and 36°N) are larger in absolute value by as much as 50%.

The latitude of zero wind stress curl approximately defines the transition from subtropical to subpolar gyre circulation, and is thus an important feature of the zonal average wind stress curl. The QSCAT-only dataset locates the zero wind stress curl line at about 50°N, some 4° to 6° farther north than in the other datasets (Fig. 2). This higher-latitude boundary between subtropical and subpolar gyre circulations is not consistent with observations and long-term average syntheses of the large-scale ocean circulation (e.g., see Schmitz 1996 for a

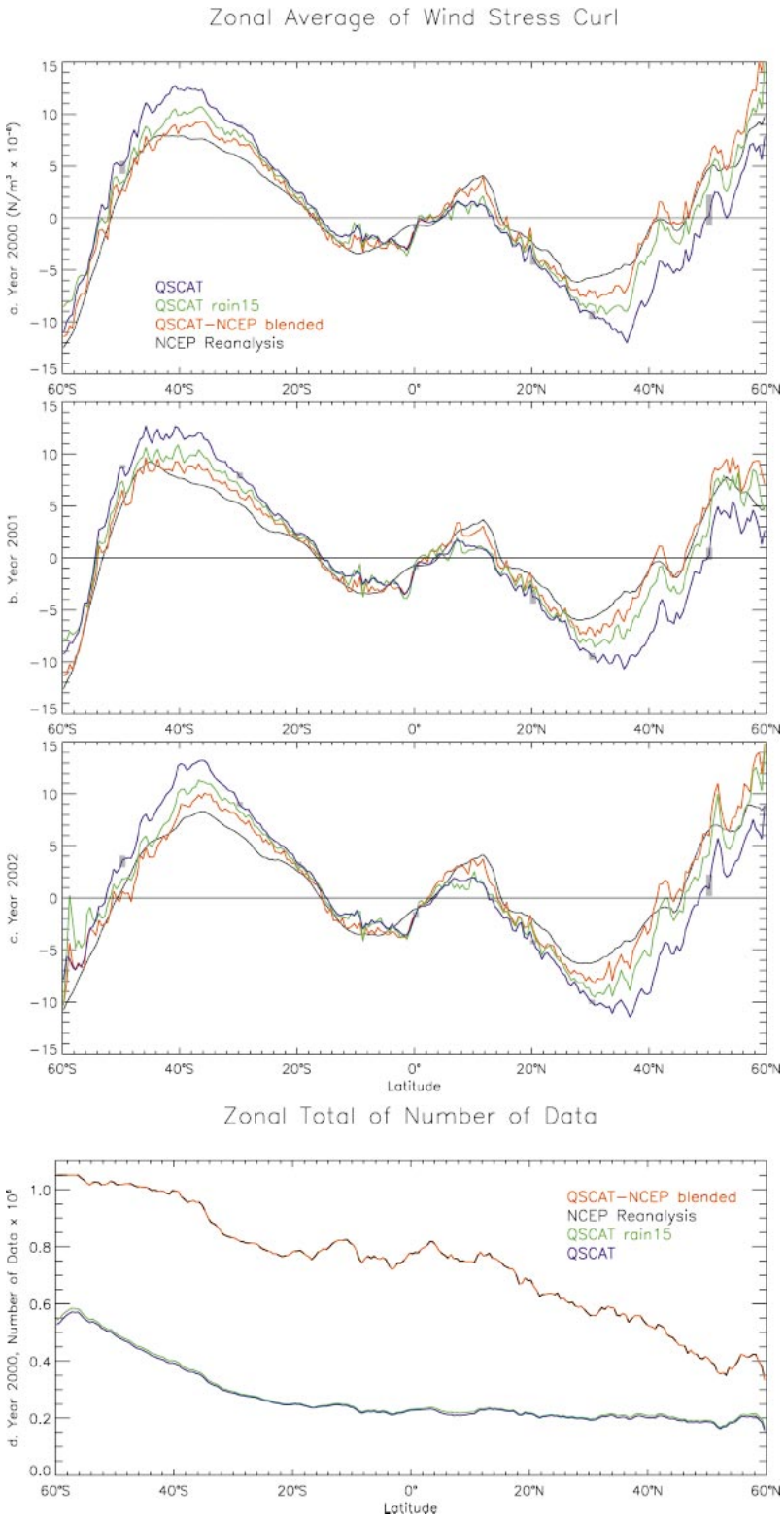

FIG. 2. Zonal and annual average wind stress curls for (a) 2000, (b) 2001, (c) 2002, and (d) the number of wind stress curls averaged as a function of latitude and dataset. The blue lines in (a)–(c) are the zonal annual average wind stress curl computed from the QSCAT-only dataset black lines are for the NCEP reanalysis case, and red lines are for

summary). Moreover, the Sverdrup balance (1) should yield an estimate of the transition latitude that is equatorward of the actual location, since (1) does not account for inertial effects of the western boundary circulation that should drive the actual subtropical/subpolar boundary poleward in the Northern Hemisphere. The high latitudes of the Northern Hemisphere zero crossings in the QSCAT-only wind stress data in Fig. 2 are thus extremely questionable.

Repeatable differences in zonal annual average wind stress curl also occur every year in the Tropics. At the equator, wind stress curl averages coincide for the three datasets, and the estimated uncertainty in the QSCAT-only amplitude is small. Just south of the equator (from 0° to 2°S) the blended QSCAT+NCEP and QSCAT-only averages are in close agreement, while the NCEP reanalysis average appears as an outlier in this region. Milliff and Morzel (2001) point out wind stress curl features in this region from their analyses of the 9-month average from NSCAT that are narrow in latitude and extend across large portions the eastern Pacific and Atlantic ocean basins. Milliff et al. (1999) demonstrated that ocean general circulation model (OGCM) response to high-wavenumber wind stress and wind stress curl forcing in this region was more realistic than to forcing derived from NCEP reanalysis alone. North of the equator, in the region 2° to 10°N that bounds the latitudes of seasonal migration of the intertropical convergence zones (ITCZ), the QSCAT-only wind stress curl average is significantly smaller than the averages for NCEP reanalysis and blended QSCAT+NCEP. The ITCZ are regions of frequent and intense rain, and we can expect the scatterometer data record to be more depleted there than anywhere else in the World Ocean.

b. Distributions

Wind stress curl zonal averages for QSCAT-only, NCEP reanalysis, and the blended QSCAT+NCEP datasets differ in regions where rain effects can play a role. To isolate the rain versus no-rain effect on wind stress curl, we examine distributions at several latitudes from the QSCAT-only and the OSU–NCEP–FNL datasets. Figure 3a shows the histograms for wind stress curl amplitudes, derived from these three swath-based surface wind datasets, in the latitude band 41° to 44°N for the calendar year 2000 (note logarithmic scale on the ordinate). Wind stress curl amplitudes (both signs) are largest in the QSCAT-only dataset, and the QSCAT-only histogram differs most from the OSU–NCEP–FNL datasets at the largest amplitudes. The differences between the OSU–NCEP–FNL histograms are smaller, with the ''rain'' case distributing over slightly larger positive wind stress curl amplitudes than for the ''no rain'' case. Each of the histograms in Fig. 3a is skewed toward positive wind stress curl, with the skewness least evident in the QSCAT-only case. This skewness is evident in the dashed lines on the positive wind stress curl

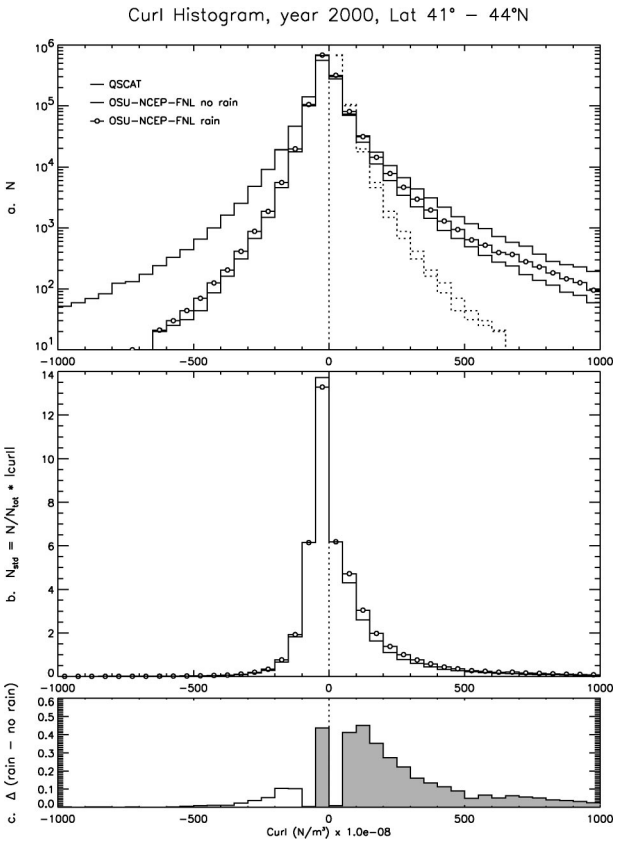

FIG. 3. Wind stress curl histograms for the calendar year 2000 in the latitude band 41°–44°N for the QSCAT-only (thick line), OSU–NCEP–FNL with rain WVCs included (thin line with bubble), and OSU–NCEP–FNL with rain WVCs excluded (thin line). In (a), the histograms are depicted using a logarithmic ordinate. In (b), the OSU–NCEP–FNL datasets are normalized by the different total numbers of wind stress curls in each distribution; OSU–NCEP–FNL with rain WVCs included contains 1 279 775 curls, and OSU–NCEP–FNL excluding the rain-flagged WVCs contains 1 217 488 curls. Each wind stress curl bin is multiplied by the curl magnitude value for the bin center (absolute values of the standardized distributions are plotted). (c) The difference of the standardized histograms in (b), ''rain included'' minus ''rain excluded.'' Bins are shaded in the difference histogram for which the difference is positive. A bias toward positive wind stress curl in the rain-flagged WVCs for this latitude band is evident.

←

FIG. 2. (*Continued*) the blended QSCAT+NCEP. The latter two datasets occur 4 times daily on regular 0.5° grids and thus contribute more wind stress curls to each zonal annual average [red line in (d)], than does the QSCAT-only dataset [blue line in (d)]. Approximate confidence intervals are computed in (a)–(c) from a bootstrap method described in the text. The green lines in (a)–(c) are the zonal annual average for QSCAT-only data when rain-flagged WVCs with wind speeds $\geq$15 m s^{-1} are also included (see section 6).

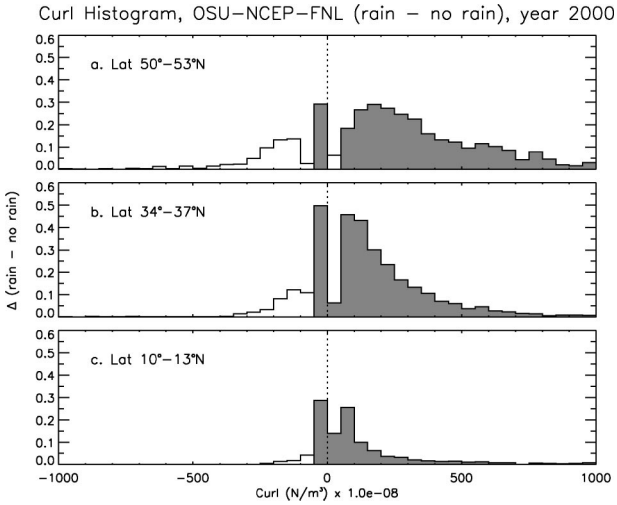

FIG. 4. Standardized wind stress curl difference histograms for the latitude bands (a) 50°–53°N, (b) 34°–37°N, and (c) 10°–13°N, computed as in Fig. 3c.

side of Fig. 3a that indicate what would be symmetric distributions for the OSU–NCEP–FNL datasets with respect to the distributions on the negative wind stress curl side of the figure.

Larger-amplitude (positive and negative) wind stress curl events in the QSCAT-only distribution are consistent with the kinetic energy differences exhibited in Fig. 1. The skewness in the OSU–NCEP–FNL distributions toward positive wind stress curl in this Northern Hemisphere latitude band (Fig. 3) is consistent with strong cyclonic systems being the principal meteorological sources for this bias. The relative absence of the skewness toward positive wind stress curl in the QSCAT-only distributions is consistent with the rain flag preferentially affecting raining cyclonic systems, thereby excluding large-amplitude positive wind stress curl events from the distribution in the Northern Hemisphere.

In Fig. 3b, the OSU–NCEP–FNL histograms have been standardized. First each histogram bin total was normalized by the respective dataset totals (e.g., 1 279 775 wind stress curl amplitudes in the ''rain'' case, 1 217 488 in the ''no rain'' case). Then the normalized bin totals were rescaled in each bin by multiplying the bin total times the curl amplitude at the center of each bin. In this standardization, the area under the curve for each bin is proportional to the contribution from each bin to the annual average wind stress curl in the given latitude band. An added population of positive wind stress curl amplitudes is evident for the dataset that included rain-flagged WVCs (line with ''bubble'' in Figs. 3a and 3b). The histogram of the difference in the standardized bin totals (''rain'' minus ''no rain'') is plotted in Fig. 3c. The bias toward missing positive wind stress curl due to rain is made clear.

Similar standardized histogram difference comparisons are shown in Fig. 4 for the latitude bands; 50°–53°N (Fig. 4a), 34°–37°N (Fig. 4b), and 10°–13°N (Fig. 4c). In all these Northern Hemisphere cases, the positive wind stress curl bias in the differences associates with the rain-flagged WVCs. Cyclonic wind stress curl in the Southern Hemisphere is of opposite (i.e., negative) sign. There, we expect the rain flag to be excluding large-amplitude, negative wind stress curls.

Figure 5 is a global map of the average wind stress curl differences computed from the OSU–NCEP–FNL datasets (''rain'' minus ''no rain'') for 2000. The hemispheric difference is indeed evident. Large-amplitude difference regions in Fig. 5 include the storm tracks of the Northern Hemisphere (e.g., 35°–50°N, emanating from western boundaries in both ocean basins), storm tracks in the Southern Hemisphere [e.g., 35°–50°S, the ITCZ in the eastern tropical Pacific (0°–10°N)], and tropical cyclone regions of the Indian and western Pacific Oceans.

The amplitudes of the wind stress curl differences in these analyses are probably underestimated by the OSU–NCEP–FNL datasets. Recall from Fig. 1 that high-wavenumber PSD is deficient in these datasets on the 50–100-km scales of the wind stress curl grid. Note also, the larger number of large-amplitude wind stress curls implied by the QSCAT-only dataset (Fig. 3a). However, wind stress curl difference distributions from the realistic high-wavenumber wind stress curl datasets (QSCAT and blended QSCAT+NCEP) cannot readily be compared. The blended QSCAT+NCEP winds substitute spectrally enhanced NCEP reanalysis surface wind vectors in the rain-flagged WVC locations. But the spectral enhancement is not sophisticated enough to be faithful to organized structures (e.g., eddies, fronts) in the surface wind field on scales just larger than a single WVC. As such, wind stress curl on the grid scale as derived from the blended QSCAT+NCEP winds in the rain-flagged and swath-gap regions will be reflective of a stochastic process other than the atmospheric physics that determine vorticity distributions at 0.5° resolution. In this sense, the OSU–NCEP–FNL datasets, while comparably deficient in PSD at high wavenumbers (Fig. 1), are consistent with respect to the physical processes leading to wind stress curl signals at the native resolutions of these data (i.e., for scales larger than about 500–600 km).

4. Synoptic setting

By emphasizing wind stress curl differences in the storm tracks and tropical cyclone regions, Fig. 5 indicates the synoptic settings that are the source of the rain-flag bias in wind stress curl from QSCAT. Figure 6 provides a midlatitude example of the spatial distribution of rain-flagged WVCs for a typical propagating low pressure system in the Pacific basin. Figure 6a depicts the OSU–NCEP–FNL interpolated winds in swaths from portions of three consecutive ascending orbits spanning the North Pacific on 31 January 2000. The time between adjacent

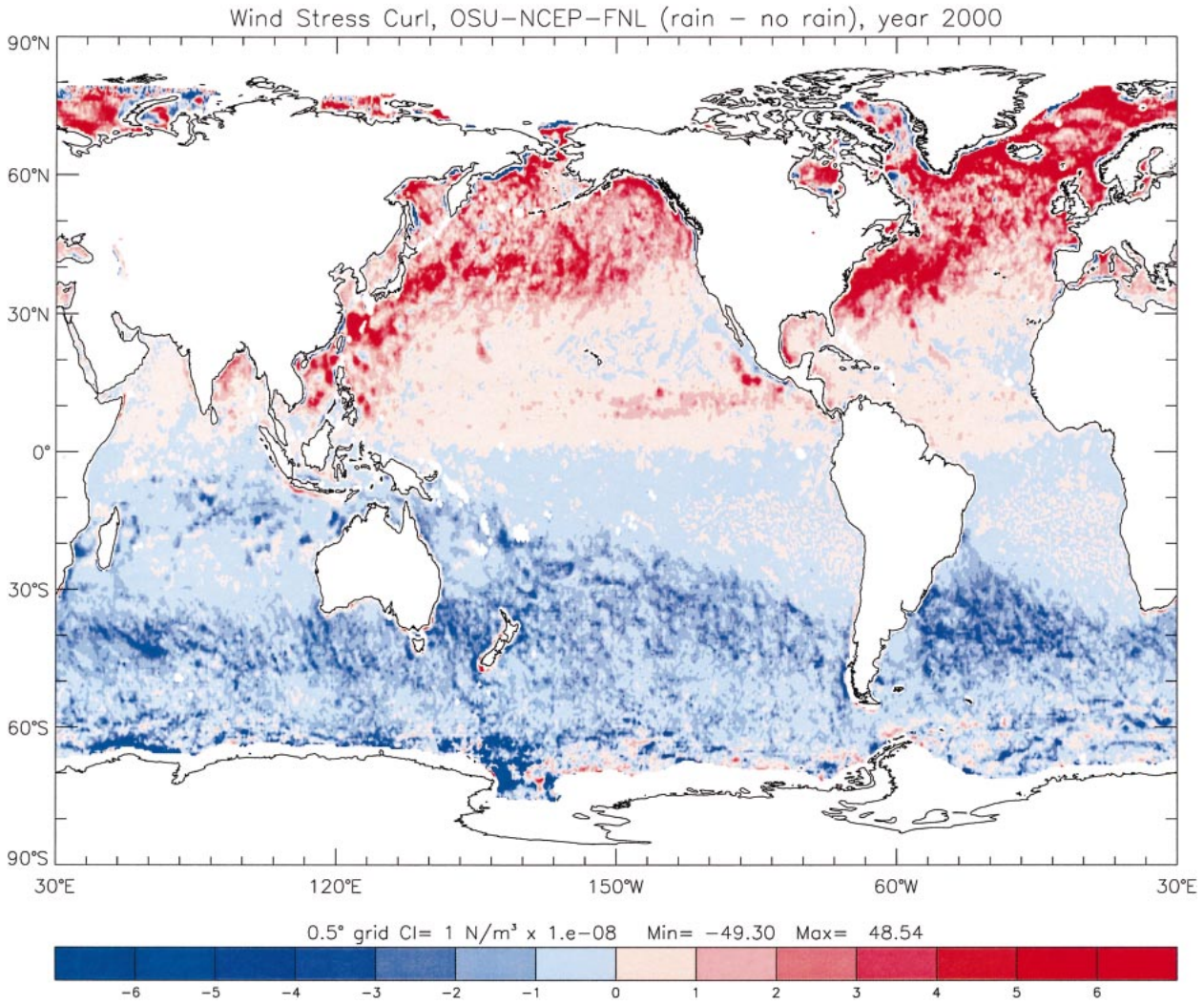

FIG. 5. Global distribution of the annual average wind stress curl difference; OSU–NCEP–FNL rain included minus OSU–NCEP–FNL rain excluded for the calendar year 2000. The rain-flagged WVCs in the Northern (Southern) Hemisphere are dominantly positive (negative). Large magnitude differences occur in storm track regions in both hemispheres and in regions of tropical convergence.

orbits is about 101 min so the total time period represented in Fig. 6 is about 3.4 h, with the most recent swath occurring in the far western Pacific.

Rain-flagged WVCs in the QSCAT record for the swaths in Fig. 6a are indicated in red. Rain-flagged WVCs clearly organize along the frontal system emanating from a low pressure center at about 50°N, 173°E. Rain-flagged WVCs also collect ahead of the main front, to the southeast of the low pressure center, consistent with rainband features that are classically associated with propagating frontal systems. There are rain-flagged WVCs associated with weaker low pressure systems in the eastern North Pacific, just out of the field of view in the figure.

The synoptic distribution of rain-flagged WVCs in Fig. 6a is not surprising; that is, rain-flagged WVCs are concentrated where it is raining. These are also the locations where wind stress curl reaches very large amplitudes, over very short spatial scales. Figure 6b depicts the wind stress curl field for the same swaths and synoptic event in Fig. 6a, as computed from the OSU–NCEP–FNL dataset that includes winds at rain-flagged locations. Wind stress curl extrema occur in the region of the low pressure center, as well as along the associated frontal system to the south. The wind stress curl signature across the front contains two extrema, one of each sign, in the latitude band 34°–41°N.

Figure 6c depicts the wind stress curl computed from QSCAT-only data for the same three swaths in Figs. 6a and 6b. Consistent with the high-wavenumber fidelity of the QSCAT data, the wind stress curl features of the synoptic system are more sharply resolved and of a larger amplitude (peak values are about a factor of 5 stronger in this example) than for the OSU–NCEP–FNL data. Also apparent is the effect on the wind stress curl analysis of WVCs missing due to rain flags in the

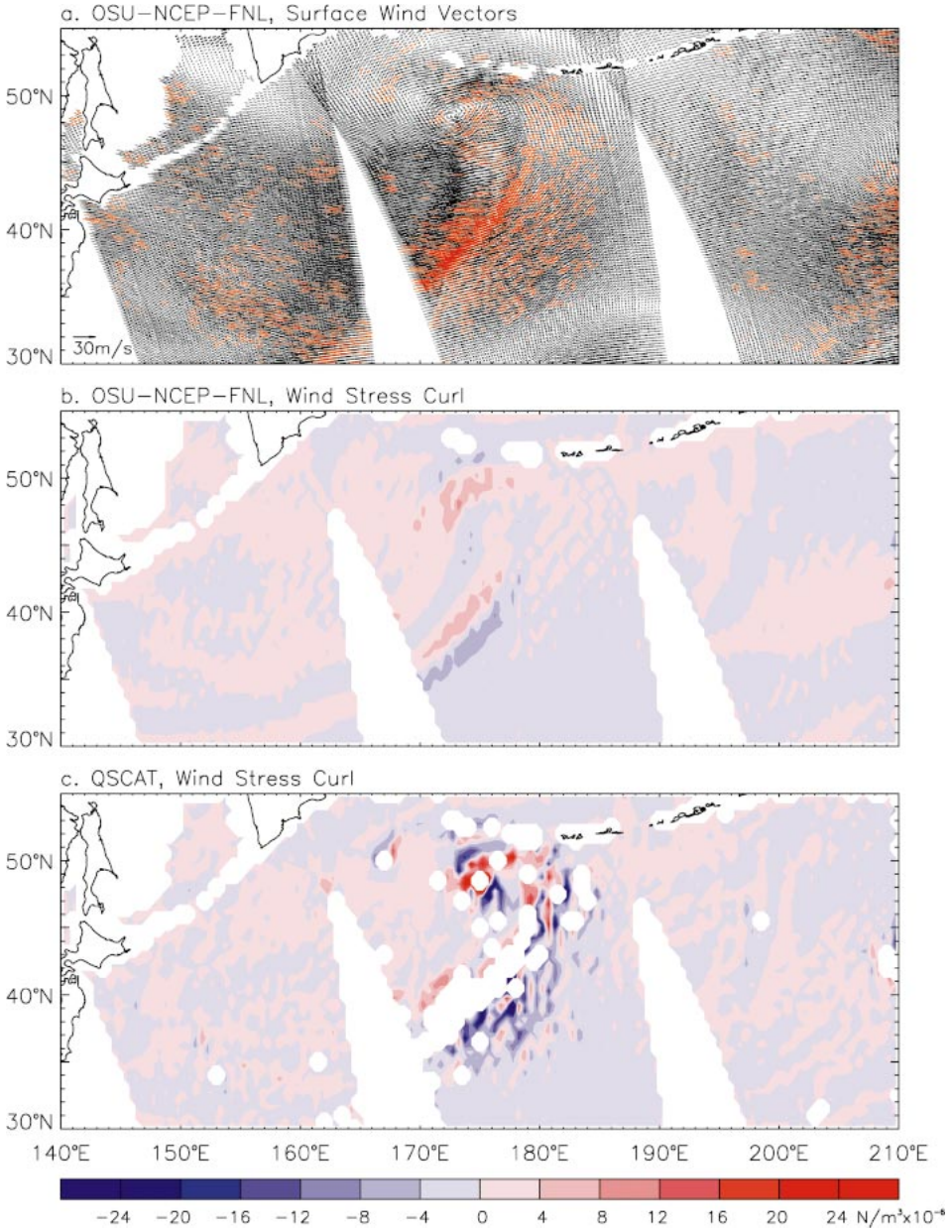

FIG. 6. A typical 5-h sample of a synoptic event occurring in the North Pacific on 31 Jan 2000. (a) Surface wind vectors from the OSU–NCEP–FNL datasets. The WVC locations that are rain flagged in the QSCAT-only data are indicated with red wind vectors. (b) Wind stress curl analysis for the same swaths using the ''rain included'' OSU–NCEP–FNL winds [i.e., black and red wind vectors in (a)]. (c) Wind stress curl analysis derivable from the QSCAT-only data for the same event.

QSCAT-only data. The large positive wind stress curls associated with the frontal feature evident in Fig. 6b are not evident in Fig. 6c. Large negative wind stress curls in Fig. 6c are less affected by the dropouts due to rain flags. These effects are apparent in the wind stress curl analyses at the relatively high resolution (e.g., 0.5°) used here.

The rain-flag biases are not apparent in 2° aggregations of wind stress curl using these same datasets for comparison. But this is little consolation given demonstrated ocean model sensitivities to realistic, high-wavenumber amplitudes in the surface wind forcing (e.g., Chen et al. 1999; Chin et al. 1998; Kelly et al. 1999; Milliff et al. 1996, 1999).

5. Wind stress divergence

Orbit-by-orbit wind stress divergence was also computed from the 50-km-binned wind stresses used to compute wind stress curl. Wind stress divergence has no

analog to the dynamical connection between basin-scale circulation and zonal integrals of the wind stress curl (1). However, extremes in averaged wind stress divergence highlight regions of important air–sea interactions where SST modifies the overlying wind field. Local feedbacks then modify the upper-ocean thermodynamics (Chelton et al. 2004). These effects have been analyzed in the tropical instability wave regime of the eastern tropical Pacific (Chelton et al. 2001), and over the Southern Ocean (O'Neill et al. 2003; P. Niiler 2003, personal communication).

Zonal, annual averages

Figure 7 demonstrates that discrepancies in zonal annual average wind stress divergence also exhibit a rain-flag bias effect in the QSCAT-only data. Confidence interval estimate procedures and color coding are the same as for the wind-stress curl averages (Fig. 2). In contrast with the wind stress curl comparison, the zonal annual averages of NCEP reanalysis wind stress divergence (black curves) in the storm track regions fall between the curves for QSCAT-only (blue) and QSCAT+NCEP (red). This suggests that rain-flag bias effects in wind stress divergence are more sensitive to spatial resolution in the storm tracks than was the case for wind stress curl. The differences between zonal annual average wind stress divergence for QSCAT-only and blended QSCAT+NCEP can be larger than 100% (e.g., see 40°N and 40°S in all years).

There are large tropical differences in zonal annual averages of the wind stress divergence as well. The year-to-year differences, especially in the Tropics, are larger for wind stress divergence than for wind stress curl. Part of this difference is likely due to the effects of the moderate El Niño–Southern Oscillation warm event in 2002. The differences with respect to NCEP reanalysis are particularly large in the Tropics. At the equator, the zonal annual average wind stress divergence from the NCEP reanalyses differs in sign and is about 3 times smaller in amplitude (Figs. 7a,b) with respect to QSCAT-only and blended QSCAT–NCEP. Weather center reanalysis winds are suspect in the Tropics, at least partly due to 2.5° spatial resolution, which is coarser than the observed scales of equatorial gradients in surface winds and SST.

Figure 8 is the global map for 2000 of the annual average wind stress divergence difference: OSU–NCEP–FNL rain minus no rain. There is no divergence analog to the hemispheric change in sign of cyclonic wind stress curl that was evident in Fig. 6. The rain-flagged WVCs tend to occur in regions of surface convergence equatorward of 60° latitude in both hemispheres (i.e., the darker blue regions in Fig. 8). The signals in the storm track regions in Fig. 8 leading to large differences in Fig. 7 are evident. Tropical difference signals are less pronounced, again presumably due to the high-wavenumber resolution deficits of OSU–NCEP–FNL. Recall that the true spatial resolution of the NCEP–FNL is on the order of 500–600 km (Fig. 1), and this is too coarse for the narrow meridional scales in wind stress divergence near the equator.

The difference map in Fig. 8 exhibits positive differences at latitudes higher than 60° in both hemispheres. These are latitudes where coverage of the OSU–NCEP–FNL data is not uniform due to sea ice and ice-edge temporal variations. Also evident off the western coasts of India, Southeast Asia, Scandinavia, western Europe, southern South America, northern North America, and elsewhere, are signals due to differences in the Gibbs ringing artifacts that are prevalent in wind stress divergence fields from weather center analyses (see Milliff and Morzel 2001, their Fig. 12).

6. Discussion

Modern regional, basin-scale, and global ocean circulation models require realistic amplitudes of high-wavenumber surface wind and wind stress curl forcings. Wind fields based on scatterometer data contain realistic high-wavenumber energy, and as of the end of 2002, wind fields based on global operational numerical weather prediction model output did not (Fig. 1).

Figure 2 implied that linear, inviscid (i.e., Sverdrup) estimates of wind-driven ocean transports can differ by as much as 50% in midlatitude storm track regions in both hemispheres. The Sverdrup circulation is not easily separated from thermohaline and inertial components of realistic ocean flows (either from observations or in models). An absolute standard for comparing wind stress curl datasets is therefore not readily obtained. But we have used inferences based on the relative transports to uncover a rain-flag bias in the QSCAT-only winds.

Transports implied by the QSCAT-only zonal average forcing are significantly larger than those implied by NCEP reanalysis and blended QSCAT+NCEP. If the NCEP reanalysis zonal averages alone were smaller, the increase in implied transport might be explained as resulting solely from realistic high-wavenumber energy in the scatterometer winds. Two other results from Fig. 2 confound this simple interpretation, however. First, the blended QSCAT+NCEP winds retain realistic high-wavenumber energy (Fig. 1), but nonetheless lead to ocean transport estimates similar to the NCEP reanalysis (Fig. 2). Second, the boundary between subtropical and subpolar ocean transports in the Northern Hemisphere as calculated from the QSCAT-only dataset is unrealistically displaced northward to latitudes inconsistent with historical ocean observations.

These findings likely result from rain-flag effects on wind stress curl distributions across several surface wind datasets. Figure 3 notes that the QSCAT-only wind stress curl distribution is anomalously symmetric with respect to the OSU–NCEP–FNL wind stress curls, with and

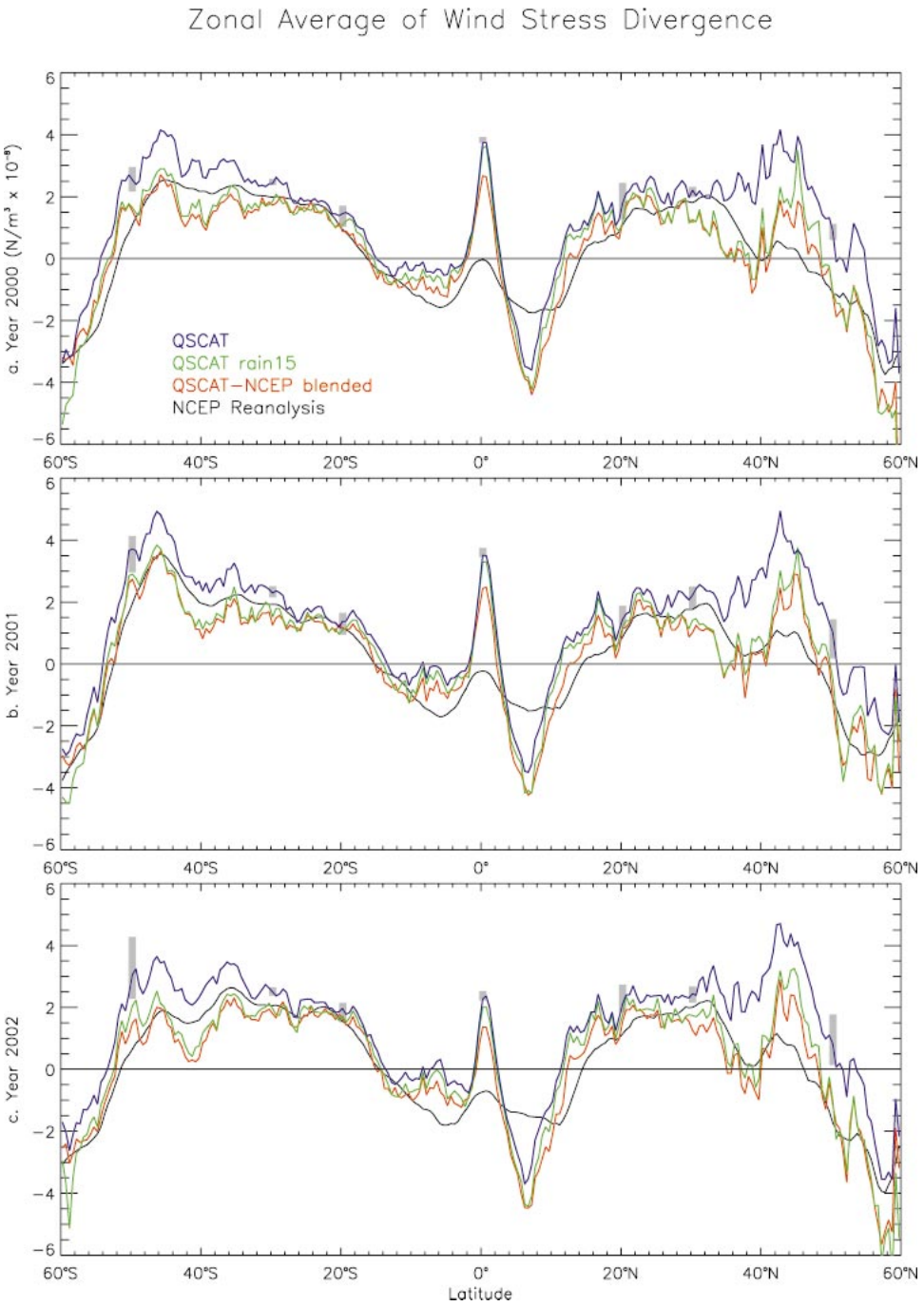

FIG. 7. Zonal annual average wind stress divergence for the calendar years (a) 2000, (b) 2001, and (c) 2002, from QSCAT-only (blue), blended QSCAT+NCEP (red), NCEP reanalysis (black), and QSCAT-only including rain-flagged WVCs for wind speeds $\geq$15 m s^{-1} (green). Confidence interval estimates for the QSCAT-only curve are computed as in Fig. 2. The large spread in the confidence interval estimate at 20°N is mostly due to near-coastal effects on wind stress divergence, principally at island boundaries (not shown).

without the rain-flagged WVCs. Distributions for the OSU–NCEP–FNL datasets are skewed toward positive wind stress curl for the Northern Hemisphere latitude band analyzed in Fig. 3. This latitude band includes large parts of the Northern Hemisphere storm tracks over the oceans; regions where we can expect rain-flag effects on QSCAT-only data to be large.

Figure 4 quantifies consistent rain-flag effects in several Northern Hemisphere latitude bands. Rain-flagged WVCs preferentially occur in regions of cyclonic wind

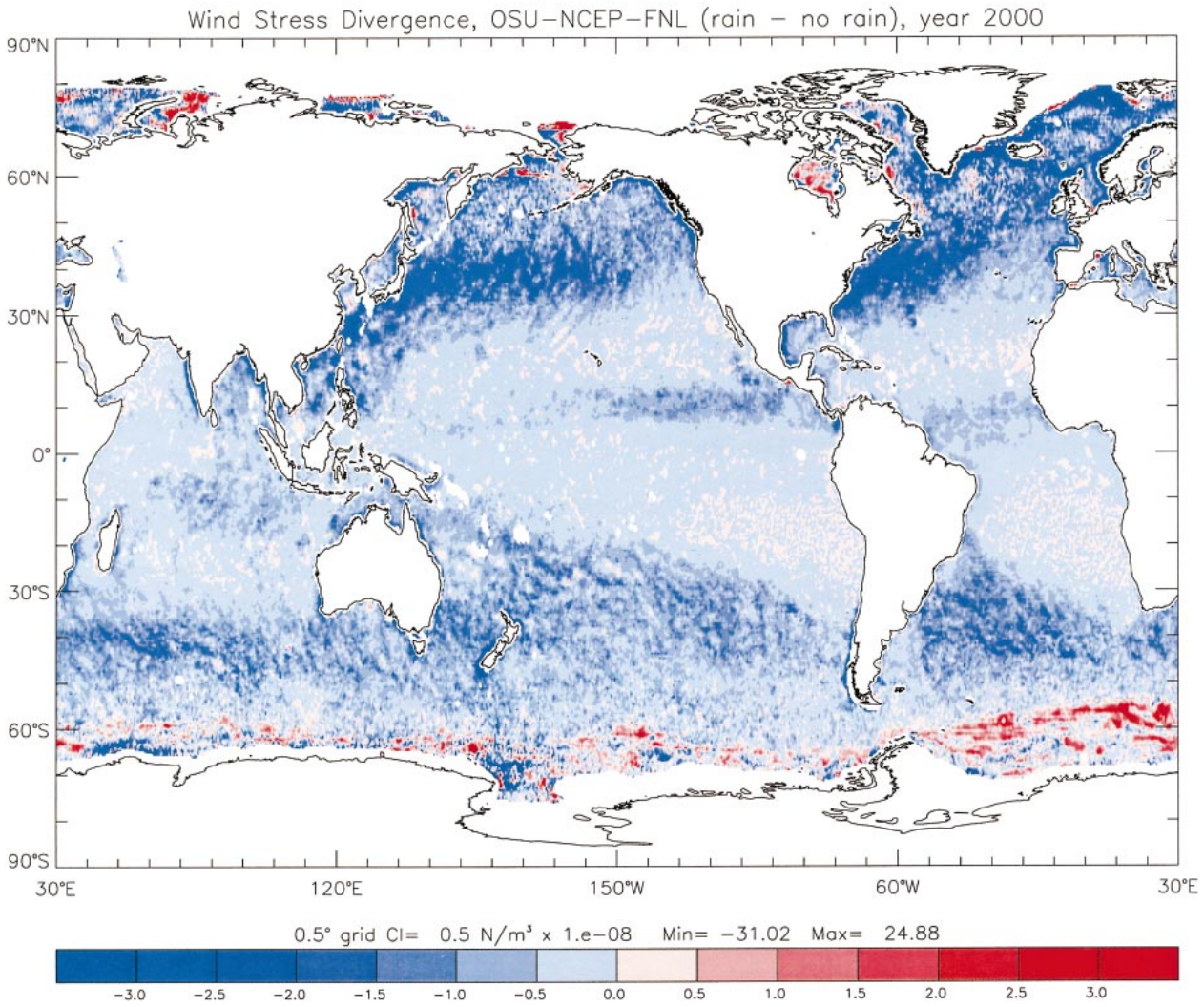

FIG. 8. Global distribution of the annual average wind stress divergence difference; OSU–NCEP–FNL rain included minus OSU–NCEP–FNL rain excluded for the calendar year 2000 (as in Fig. 5 for wind stress curl). Large magnitude differences occur in storm track regions of both hemispheres. Possible sampling artifacts due to seasonal ice cover lead to positive differences in high latitudes.

stress curl, and the wind stress curl amplitudes in these regions can be large. In Fig. 5 there is a striking change in sign across the equator, consistent with the change in the sense of cyclone rotation. Storm track regions in both hemispheres are highlighted in Fig. 5, adding support to the premise that large-amplitude wind stress curls occur in raining, cyclonic systems.

The impact of the correlation between cyclonic wind stress curl and rain is demonstrated for a typical synoptic system in the North Pacific (Fig. 6). Two features of the excluded wind stress curls depicted in Fig. 6 are important to note. First, the across-front spatial scale is small and consistent with the high-wavenumber region in Fig. 1 that distinguished surface wind datasets containing scatterometer wind information from those that did not. Second, the amplitudes of the wind stress curls from the scatterometer data are much larger than the OSU–NCEP–FNL counterparts. As such, the rain-flag bias inferences we draw from wind stress curl distribution differences based on OSU–NCEP–FNL winds (e.g., Figs. 3–5) are underestimates of the true effect.

The essential properties of a better surface wind forcing dataset for the purposes of ocean modeling include both realistic high-wavenumber amplitudes in wind stress curl, and an amelioration of the rain-flag bias inherent in scatterometer-only surface wind retrievals. We have noted that the blended QSCAT+NCEP winds are a step in this direction. The spectral character of the blended QSCAT+NCEP winds is constrained to approximate that of the QSCAT-only data, on regional and monthly scales. Rain-flagged WVCs are supplanted with spectrally augmented winds based on coincident NCEP analyses. However, the spectral augmentation of NCEP analyses contains a random component (Chin et al.

1998) that cannot reproduce realistic space–time character of synoptic systems (e.g., propagating fronts) where large-amplitude wind stress curls are found.

We suggest below that realistic wind stress curl amplitudes in propagating synoptic systems are more appropriately obtained on time scales resolved by the Tandem Mission. In the meantime, progress in correcting biases in a single scatterometer observing system can be made through more sophisticated assignments of rain flags in high wind speed regimes. To support this assertion, we have modified the blended QSCAT+NCEP winds to include QSCAT winds, irrespective of rain flag, when the retrieved wind speed is 15 m s^{-1} or faster. Implied Sverdrup transports due wind stress curls computed from this modified wind dataset are depicted by green curves in Fig. 2, labeled QSCAT-rain15. Not surprisingly, larger wind speed amplitudes lead to larger wind stress curl amplitudes, and the implied ocean transports in Fig. 2 are enhanced with respect to the curves (red) for QSCAT+NCEP blended product discussed in section 3. However, the QSCAT-rain15 curve also results in a more acceptable latitude for the boundary between implied subtropical and subpolar transports. This suggests that the increase in implied transports for QSCAT-rain15 are not a side effect of a rain-flag bias.

The 15 m s^{-1} threshold in this modified product is guided by QSCAT rain-flagged surface wind retrieval comparisons with National Data Buoy Center (NDBC) buoy winds reported by Freilich and Vanhoff (2003). Their comparison implied that the QSCAT rain-flag algorithm incorrectly identifies rain contamination in a significant number of retrievals when NDBC buoy wind speeds are 15 m s^{-1} or greater.

The QSCAT-rain15 winds have also been used to compute zonal averages of wind stress divergence. As was the case for wind stress curl, the QSCAT-rain15 amplitudes lie between blended QSCAT+NCEP and the QSCAT-only curves for almost all latitudes. Unlike the wind stress curl case, QSCAT-rain15 zonal average divergence is much closer to blended QSCAT+NCEP over middle and high latitudes. Conversely, within 2° of the equator, the QSCAT-rain15 zonal averages of wind stress divergence are very similar to the QSCAT-only zonal averages. Zonal averages of wind stress divergence are not as sensitive to missing high-speed winds due to rain flags in middle and high latitudes. But in strongly divergent surface wind regimes on the equator, there is evidence that some high-wind events are erroneously excluded from the QSCAT record due to rain flags. Note that in the low-latitude region of the ITCZ, where heavy rains are common, the QSCAT-rain15 zonal-average wind stress divergence matches the blended QSCAT+NCEP curve. This suggests that in these strongly convergent regions, the rain flag is operating as intended.

In future work, we will examine rain-flag effects during the 6-month record for the Tandem Mission. Given two scatterometer systems, almost all swath-gap regions unsampled in one 6-h time window are covered in the succeeding 6 h (Schlax et al. 2001). Within each 6-h window, the swath-gap regions will be minimized, and the preservation of short spatiotemporal scale variability in the wind stress curl and divergence fields is enhanced by almost a factor of 2. For the small remaining swath-gap regions and missing data within the swaths, the blending method developed by Chin et al. (1998) will be useful in removing the wind stress curl and divergence biases due to rain effects on surface wind retrievals from scatterometer observations, and providing a realistic high-wavenumber regularly gridded surface wind dataset sufficient to force modern ocean models. We acknowledge that for purposes other than forcing modern ocean models, different design decisions might be appropriate in the construction of uniform global or regional surface wind and surface wind derivative fields, based on scatterometer data.

7. Conclusions

Scatterometer data provide essential resolution of energetic surface winds in propagating synoptic systems. However, heavy rain that accompanies these systems degrades the quality of surface wind retrievals from scatterometer data, leading to biases in distributions of wind stress curl and divergence. Zonal averages of the biased wind stress curl infer erroneous Sverdrup transports by as much as 50% in storm-track regions in both hemispheres. There is evidence that the rain-flag algorithm used in processing scatterometer data is too conservative at high wind speeds. A surface wind dataset that blends scatterometer and weather center surface wind analyses is shown to ameliorate some of the rain-flag bias effects in zonal averages of wind stress curl and wind stress divergence. More faithful representation of the true synoptic variability in surface winds could be obtained with a second scatterometer instrument (i.e., a Tandem Mission), and an improved rain-flag algorithm.

Acknowledgments. The authors are pleased to acknowledge research support from the NASA Ocean Vector Winds Science Team. We thank Dr. Barry Vanhoff for facilitating access to the OSU–NCEP–FNL product.

REFERENCES

Chelton, D. B., and Coauthors, 2001: Observations of coupling between surface wind stress and sea surface temperature in the eastern tropical Pacific. *J. Climate,* **14,** 1479–1498.

——, M. G. Schlax, M. H. Freilich, and R. F. Milliff, 2004: Satellite radar measurements reveal short-scale features in the wind stress field over the world ocean. *Science,* **303,** 978–983.

Chen, D., W. T. Liu, S. E. Zebiak, M. A. Cane, Y. Kushnir, and D. Witter, 1999: Sensitivity of the tropical Pacific Ocean simulation to the temporal and spatial resolution of wind forcing. *J. Geophys. Res.,* **104C,** 11 261–11 271.

Chin, T. M., R. F. Milliff, and W. G. Large, 1998: Basin-scale, high wavenumber, sea surface wind fields from a multiresolution anal-

ysis of scatterometer data. *J. Atmos. Oceanic Technol.,* **15,** 741–763.

Draper, D. W., and D. G. Long, 2002: An assessment of SeaWinds on QuikSCAT wind retrieval. *J. Geophys. Res.,* **107C,** 3212, doi: 10.1029/2002JC001330.

Ebuchi, N., H. C. Graber, and M. J. Caruso, 2002: Evaluation of wind vectors observed by QuikSCAT/SeaWinds using ocean buoy data. *J. Atmos. Oceanic Technol.,* **19,** 2049–2062.

Freilich, M. H., 1996: Sea winds algorithm theoretical basis document. Jet Propulsion Laboratory, California Institute of Technology, Pasadena, CA, 56 pp. [Available online at http://podaac.jpl.nasa.gov/quikscat/qscat_doc.html.]

——, and D. B. Chelton, 1986: Wavenumber spectra of Pacific winds measured by the Seasat scatterometer. *J. Phys. Oceanogr.,* **16,** 741–757.

——, and B. Vanhoff, 2003: The accuracy of the QuikSCAT Standard (L2B and DIRTH) wind products. *Proc. Ocean Vector Winds Science Team Meeting,* Oxnard, CA, NASA Jet Propulsion Laboratory.

Huddleston, J. N., and B. W. Stiles, 2000: Multidimensional Histogram (MUDH) Rain Flag, Product description version 2.1. Jet Propulsion Laboratory, California Institute of Technology, Pasadena, CA, 8 pp.

Kalnay, E., and Coauthors, 1996: The NCEP/NCAR 40-Year Reanalysis Project. *Bull. Amer. Meteor. Soc.,* **77,** 437–471.

Kelly, K. A., S. Dickinson, and Z. Yu, 1999: NSCAT tropical wind stress maps: Implications for improving ocean modeling. *J. Geophys. Res.,* **104C,** 11 291–11 310.

Mears, C., F. Wentz, and D. Smith, 2000: SeaWinds on QuikScat Normalized Objective Function Rain Flag, Product description version 1.2. Remote Sensing Systems, Santa Rosa, CA, 13 pp.

Milliff, R. F., and J. Morzel, 2001: The global distribution of the time-average wind-stress curl from NSCAT. *J. Atmos. Sci.,* **58,** 109–131.

——, W. G. Large, W. R. Holland, and J. C. McWilliams, 1996: The general circulation responses of high-resolution North Atlantic ocean models to synthetic scatterometer winds. *J. Phys. Oceanogr.,* **26,** 1747–1768.

——, ——, J. Morzel, G. Danabasoglu, and T. M. Chin, 1999: Ocean general circulation model sensitivity to forcing from scatterometer winds. *J. Geophys. Res.,* **104C,** 11 337–11 358.

——, M. H. Freilich, W. T. Liu, R. Atlas, and W. G. Large, 2001: Global ocean surface vector wind observations from space. *Observing the Oceans in the 21st Century,* C. J. Koblinsky and N. R. Smith, Eds., GODAE Project Office and Bureau of Meteorology, 102–119.

National Aeronautics and Space Administration, 2001: QuikSCAT science data product user's manual, overview and geophysical data products, version 2.2. Jet Propulsion Laboratory, California Institute of Technology, Pasadena, CA, 89 pp. [Available online at http://podaac.jpl.nasa.gov/quikscat/qscat_doc.html.]

National Research Council, Space Studies Board, 2000: *Ensuring the Climate Record from the NPP and NPOESS Meteorological Satellites.* National Academy Press, 51 pp.

Nonaka, M., and S.-P. Xie, 2003: Covariations of sea surface temperature and wind over the Kuroshio and its extension: Evidence for ocean–atmosphere feedback. *J. Climate,* **16,** 1404–1413.

O'Neill, L. W., D. B. Chelton, and S. K. Esbensen, 2003: Observations of SST-induced perturbations of the wind stress field over the Southern Ocean. *J. Climate,* **16,** 2340–2354.

Patoux, J., and R. A. Brown, 2001: Spectral analysis of QuikScat surface winds and two-dimensional turbulence. *J. Geophys. Res.,* **106D,** 23 995–24 005.

Pedlosky, J., 1998: *Ocean Circulation Theory.* 1st ed. Springer-Verlag, 453 pp.

Schlax, M. G., D. B. Chelton, and M. H. Freilich, 2001: Sampling errors in wind fields constructed from single and tandem scatterometer datasets. *J. Atmos. Oceanic Technol.,* **18,** 1014–1036.

Schmitz, W. J., 1996: On the circulation of the world ocean: Vol. 1, Some global features/North Atlantic circulation. WHOI Tech. Rep. 96-03, 150 pp.

Stiles, B. W., 1999: Special wind vector data product: Direction interval retrieval with thresholded nudging (DIRTH), Product description version 1.1. Jet Propulsion Laboratory, California Institute of Technology, Pasadena, CA, 9 pp.

Wikle, C. K., R. F. Milliff, and W. G. Large, 1999: Surface wind variability on spatial scales from 1 to 1000 km observed during TOGA COARE. *J. Atmos. Sci.,* **56,** 2222–2231.